Analysis of *p*-Type Doping in Graphene Induced by Monolayer-Oxidized TMDs

Tuyen Huynh,[#] Tien Dat Ngo,[#] Hyungyu Choi, Minsup Choi, Wonki Lee, Tuan Dung Nguyen, Trang Thu Tran, Kwangro Lee, Jun Yeon Hwang, Jeongyong Kim, and Won Jong Yoo*

Cite This: *ACS Appl. Mater. Interfaces* 2024, 16, 3694−3702

Read Online

ACCESS | Metrics & More | Article Recommendations | Supporting Information

ABSTRACT: Doping is one of the most difficult technological challenges for realizing reliable two-dimensional (2D) material-based semiconductor devices, arising from their ultrathinness. Here, we systematically investigate the impact of different types of nonstoichiometric solid MO_x (M are W or Mo) dopants obtained by oxidizing transition metal dichalcogenides (TMDs: WSe_2 or MoS_2) formed on graphene FETs, which results in *p*-type doping along with disorders. From the results obtained in this study, we were able to suggest an analytical technique to optimize the optimal UV-ozone (UVO) treatment to achieve high *p*-type doping concentration in graphene FETs ($\sim 2.5 \times 10^{13}$ cm^{-2} in this study) without generating defects, mainly by analyzing the time dependency of D and D' peaks measured by Raman spectroscopy. Furthermore, an analysis of the structure of graphene sheets using TEM indicates that WO_x plays a better protective role in graphene, compared to MoO_x, suggesting that WO_x is more effective for preventing the degradation of graphene during UVO treatment. To enhance the practical application aspect of our work, we have fabricated a graphene photodetector by selectively doping the graphene through oxidized TMDs, creating a *p*−*n* junction, which resulted in improved photoresponsivity compared to the intrinsic graphene device. Our results offer a practical guideline for the utilization of surface charge transfer doping of graphene toward CMOS applications.

KEYWORDS: *2D semiconductors, UV-ozone treatments, tungsten oxide, molybdenum oxide, surface charge transfer doping*
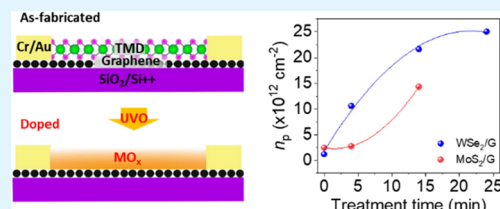
INTRODUCTION

Substitutional doping by ion implantation followed by thermal activation has been used as a very essential technology for producing commercial semiconductor devices.[1] Nonetheless, substitutional doping for two-dimensional (2D) materials is limited by their atomic thickness,[2] and substitutional dopants unmatching with 2D lattice atoms further cause substantial scattering of charge carriers which results in degraded carrier mobility.[3] Meanwhile, electrostatic doping has been used predominantly for 2D materials, by which an external electrostatic field is applied to control the doping level without changing the original lattice structures. However, the operation of transistors without dopant atoms requires a complicated design when developing industry-compatible semiconductor devices,[4−6] as various biases applied to electrodes are needed to control doping concentration as well as controlling on- and off-current flowing between source and drain. Therefore, electrostatic doping faces limitations for use in 2D material-based CMOS technology due to its complicated processing and reliability.

Surface charge transfer doping (SCTD) has recently gained great interest in the research community as a potential alternative for ion implantation due to its facile, diverse, and low-temperature processing capability.[7] In SCTD methods, solid-state dopants such as nonstoichiometric tungsten oxide (WO_x) or molybdenum oxide (MoO_x) are proposed to induce

a *p*-type doping effect on 2D materials with the advantage of CMOS processing compatibility in the environment where most of the 2D transition metal dichalcogenides (TMDs)-based pristine devices show *n*-type semiconducting properties.[8−18] Recently, our group has demonstrated an effective strategy to spatially control the doping selectively, which further accelerates the application of solid-state SCTD.[18] The solid-state dopants are formed on top of the targeted 2D materials by an oxidation process such as UV-ozone (UVO) treatment or an oxygen plasma process. However, to the best of our knowledge, systematic studies have not been conducted on defects or disorders generated during solid-state SCTD on the surface of a fragile, ultrathin body of 2D materials. Thus, a guideline for controlling doping levels and optimizing oxidation processing conditions is required.
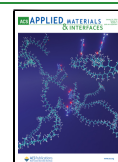
In this study, solid-state dopants such as WO_x or MoO_x formed upon oxidation of monolayer TMDs (1L-WSe_2 or 1L-MoS_2) are used to dope monolayer graphene. The UVO treatment at room temperature is utilized in this work due to

its controllable and less defective oxidation process compared to oxygen plasma treatment.[19] *P*-type doped graphene was experimentally probed through electrical measurements and Raman spectroscopy. The optimal UVO treatment durations required to achieve high-doping concentration ($\sim$2.5 $\times$ 10^{13} cm^{-2}) and nondefective graphene channel are found to be $\sim$24 and $\sim$14 min for WSe$_2$ and MoS$_2$ encapsulated samples under our processing condition, respectively. Interestingly, after further exceeding the above-mentioned treatment durations, defects, and disorders are generated during overoxidation, which is confirmed by the appearance of *D* and *D'* Raman peaks of graphene. TEM analysis reveals that graphene covered by WSe$_2$ has higher crystallinity compared to the graphene under MoS$_2$ after the same period of UVO exposure time. This suggests that WO$_x$ provides better protection to graphene against UVO treatment, as evidenced by the preservation of its crystallinity. To further enhance the practical application aspect of our work, we have further taken a significant step by fabricating a graphene photodetector. This photodetector is created by selectively doping graphene through SCTD, thereby forming a *p*−*n* junction. This innovative approach results in improved photoresponsivity compared to the intrinsic graphene device.

■ RESULTS AND DISCUSSION

Figure 1a shows a schematic of graphene FETs encapsulated by a single layer of TMDs followed by UVO treatments to
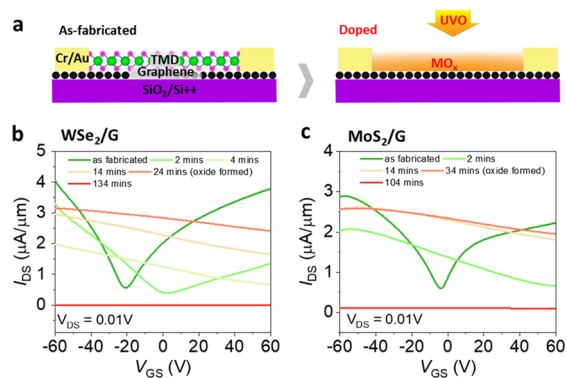
Figure 1. (a) Schematic of the device structure before and after UVO treatments. Transfer characteristics of (b) WSe$_2$- and (c) MoS$_2$-encapsulated graphene FETs, with the accumulated UVO-treatment duration.

form a nonstoichiometric oxide layer on top of the devices. The details of thickness confirmation for graphene and TMDs are represented in Figure S1. The doped graphene FETs are fabricated by stacking either 1L-WSe$_2$ or 1L-MoS$_2$ on single-layer graphene exfoliated on a heavily *p*-doped silicon substrate capped with 285 nm thick thermal SiO$_2$. Metal contacts were patterned via electron beam lithography. A plasma etching process is conducted with SF$_6$ gas on exposed graphene prior to the formation of metal contact with a Cr−Au deposition process by an electron beam evaporator. The top layer, 1L-WSe$_2$ (or 1L-MoS$_2$), is subsequently oxidized into MO$_x$ (M are W or Mo) by UVO treatment at room temperature, for varied durations (The fabrication process is detailed in the Experimental Section and Figure S2). In particular, the UVO treatment, where only chemical reactions take place,[20] can be an effective candidate for this work due to its advantages in the

controllable and less defective oxidation process (Figure S3a).[19] In contrast to UVO, the oxygen plasma oxidation mechanism is characterized by a combination of chemical reaction and physical ion bombardment,[20] leading to a considerably enhanced oxidation rate (Figure S3b).[21,22] In Figure S3c−f, we present a comparison of 1L-WSe$_2$-based graphene samples that underwent treatment using oxygen plasma and UVO treatment. This comparison highlights the significant difference in the oxidation processes between the two methods. The oxygen plasma treatment achieves rapid oxidation within a short time frame of only 20 s, in contrast to the much longer treatment duration of 24 min required for UVO treatment. Furthermore, bombardment on the 2D surface from the highly energetic oxygen ions or radicals induces lattice distortion in the treated surface.[22] It is important to notice that a possible solution can be performing soft plasma treatments on multilayer TMDs, in such a way to induce the oxidation of the topmost layers.[23] In our study, we used monolayer TMDs as an encapsulating layer. Therefore, UVO at room temperature is the superior selection, enabling facile controllability and operation.

To explore the electrical performance of doped graphene FETs, the devices are measured in a pristine state and right after every treatment. The transfer characteristics of both types of devices are shown in Figure 1b,c. Both WSe$_2$- and MoS$_2$-encapsulated graphene devices show ambipolar behavior with Dirac point located near zero gate voltage at pristine state, which reveals the high quality of our graphene devices attributing to the protection of graphene by TMDs layer preventing generation of resist residues during the fabrication process.[24] However, after 2 min of UVO treatment, the MoS$_2$-graphene device shows a degenerately *p*-type behavior, while the WSe$_2$-graphene device requires at least 4 min to show a degenerately *p*-type behavior. Interestingly, with 2 (4) min of UVO treatment, MoO$_x$ (WO$_x$) is not yet formed from MoS$_2$ (WSe$_2$), confirmed by Raman spectra of MoS$_2$ (WSe$_2$) in Figures S4 and S5. This observation reveals that doping of graphene FETs begins when the topmost monolayer TMDs is doped by oxygen atoms. The increase in hole concentration of the TMDs layer results in the shifting of their Fermi level toward the valence band, which allows more hole carriers to transfer to graphene FETs. Prolonged exposure to UVO has different effects on WSe$_2$-based devices and MoS$_2$-based graphene devices. For the WSe$_2$-based device, the longer UVO exposure of 24 min results in degenerated *p*-type transfer characteristic, and nonstoichiometric WO$_x$ is simultaneously formed (Figure S4). Further UVO exposure after the formation of oxide layers results in degradation on the on-state of the WSe$_2$-based device. On the other hand, the maximum on-current of the MoS$_2$-based graphene device is achieved after 14 min of treatment, when MoO$_x$ is still yet formed (Figure S4), and further treatment of the device results in an insignificant change in the transfer characteristic of the device. The difference in transfer characteristics of these devices will be explained in the next section regarding defects generation of TMDs encapsulated graphene during UVO treatment. Finally, both types of graphene devices are fully degraded with no current flow after 104 and 134 min of UVO treatment for MoO$_x$- and WO$_x$-based graphene devices, respectively (Figure S6).

To quantitatively probe the doping concentration of the samples, we conduct room temperature Hall effect measurements with a measurement configuration illustrated in Figure

2a, where the current I_D flows through the channel of Hall bar devices, and the Hall voltage V_H arises due to a perpendicular
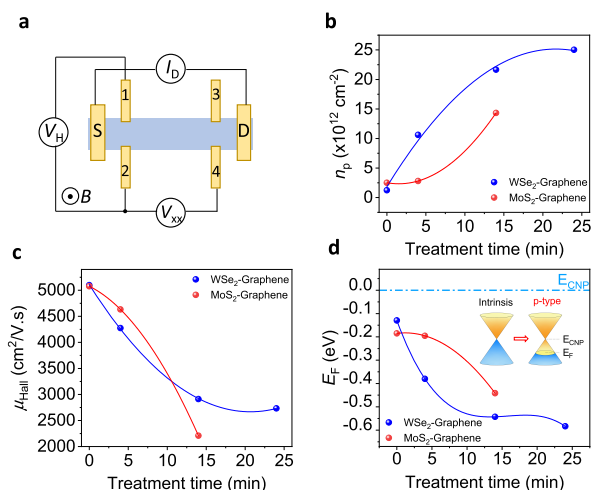
Figure 2. (a) Measurement configuration of a typical Hall bar structure device, which is used to measure (b) doping concentration and (c) room temperature Hall mobility of WSe$_2$-graphene and MoS$_2$-graphene until when the generation of defects is observed on the graphene channel. (d) Corresponding Fermi levels of graphene with respect to E_{CNP}.

magnetic field $B_z = 2$ (T) at a fixed $V_G = 0$ V. The V_H measurement allows the determination of carrier concentration, which is obtained by the following equation:[25]

$$n_{2D} = \frac{I_D \cdot \Delta B_z}{q \cdot \Delta V_H} \tag{1}$$

The Hall effect mobility is extracted from a previous study:[25]

$$\mu_H = \frac{V_H \cdot L_{4P}}{V_{xx} \cdot W \cdot B_z} \tag{2}$$

where the Hall voltage V_H is calculated from this equation: $V_H = (I_D \cdot B_z)/(q \cdot n_{2D})$.[25] L_{4P} ($L_{4P} = 4$ μm) and V_{xx} ($V_{xx} = |V_3 - V_1|$) are the distance and voltage difference between probes 1 and 3. W is the width of the channel, which is equal to 4 μm.

Figure 2b,c shows the plot of n_p and μ_H in comparison over 24 and 14 min UVO treatment duration for WSe$_2$- and MoS$_2$-based devices, respectively. We chose these treatment times for the Hall measurements because no degradation occurs on the on-state for both types of devices after the above-mentioned UVO exposure periods. We observed a significant increase of n_p for both types of encapsulated graphene FETs. The WSe$_2$-based graphene device reaches a maximum n_p of 2.5×10^{13} cm^{-2} after 24 min, while the MoS$_2$-based devices show n_p of 1.4×10^{13} cm^{-2} (after 14 min). Thus, the optimal time to obtain the highest doping concentration for graphene FETs by the oxide layer is found when WO$_x$ appears on top of WSe$_2$-encapsulated graphene; however, for MoS$_2$-encapsulated graphene, it is relatively difficult to identify a specific treatment time point that results in optimal doping concentration. This is because the carrier concentration saturates before the oxide layer appears. To highlight the novelty of our work, we have made a comparison table, as depicted in Table S1. On the other hand, Figure 2b shows the μ_H of graphene devices with varied UVO treatment times. Related to the increasing trend of n_p with both types of the devices, the room temperature

mobility of MoS$_2$- (WSe$_2$-) based graphene devices decreased from 5077 to 2210 cm^{2}V^{-1}s^{-1} (from 5098 to 2734 cm^{2}V^{-1}s^{-1}), similar to the previous reports.[11,26,27] The trade-off of μ_H against n_p can be solved by isolating the dopant layer, which is rich in scattering centers, from the channel material using an insulating layer such as hBN.[11,26,27] In addition, the thickness of encapsulating TMDs and graphene is also critical to our device performance. The influence of channel (graphene) thickness on our device performance, particularly with SCTD, aligns with the trend proposed by Arnold et al.,[28] affecting the electrostatic controllability of the bottom-gate after oxidation. An increase in the channel thickness results in minimal threshold voltage modulation (ΔV_{th}) due to weak surface potential modulation caused by weak bottom electrostatic gating. In contrast, for the thin-channel device, the charge induced by SCTD and bottom-gating is additive, therefore increasing the ΔV_{th} of the device after prolonged oxidation. The effect of thickness of the top TMDs flakes is represented by Choi et al.,[11] which shows a decrease in doping concentration while increasing the thickness of the TMDs flakes. That observation is attributed to the increase in the distance between the channel material and MO$_x$ (WO$_x$).

The doping mechanism of solid-state dopants such as nonstoichiometric MoO$_x$ (WO$_x$), formed on top of the graphene by UVO treatment, is proposed to induce a p-type doping effect on the graphene flake based on the work-function-mediated charge transfer.[11] Due to the Fermi level shift by the work-function modification, the eletrical characteristic of graphene FET turns into p-type with increased hole concentration. To further clarify the doping mechanism of SCTD, we determined the modification in the Fermi level of graphene attributed to the UVO treatment using the formula:[11]

$$E_{CNP} - E_F = \hbar \nu_F \sqrt{\pi n} \tag{3}$$

where E_{CNP} is the energy of the charge neutral point, $\hbar$ is the reduced Planck constant, ν_F is the Fermi velocity in graphene (10^6 ms^{-1}),[11] and n is the carrier concentration (extracted from Hall measurements as depicted in Figure 2c). Figure 2d shows the E_F of MoS$_2$ (WSe$_2$)-based graphene FETs before and after UVO treatment, extracted using formula 1. Due to UVO treatment, E_F of MoS$_2$-based graphene FET was modified from 4.75 to 5 eV (From 0 to 14 min of UVO treatment). For the WSe$_2$-based graphene FET, E_F decreases from 4.69 to 5.14 eV, which indicates a more effective doping concentration for WSe$_2$-based graphene FET compared to MoS$_2$-based graphene FET. Based on the obtained work function values, a diagram illustrating the Fermi level shift of graphene before and after UVO treatment of the top TMDs layer is demonstrated in Figure S7. Additionally, Kelvin probe force microscopy (KPFM) is also conducted to enhance the reliability of the calculation of the work function from n (Figure S8). We fabricated WSe$_2$-encapsulated graphene and subsequently performed KPFM after every UVO treatment period (4, 14, and 24 min). The work function of WSe$_2$-based graphene increases with a prolonged UVO treatment time, consistent with the values extracted from n.

To explain the difference in electrical performances of graphene devices covered by MoS$_2$ and WSe$_2$ undergone UVO treatment, we performed Raman spectroscopy to investigate the crystal structure transformation of graphene after a prolonged UVO treatment. Raman spectroscopy is used because it is a nondestructive method, which is able to
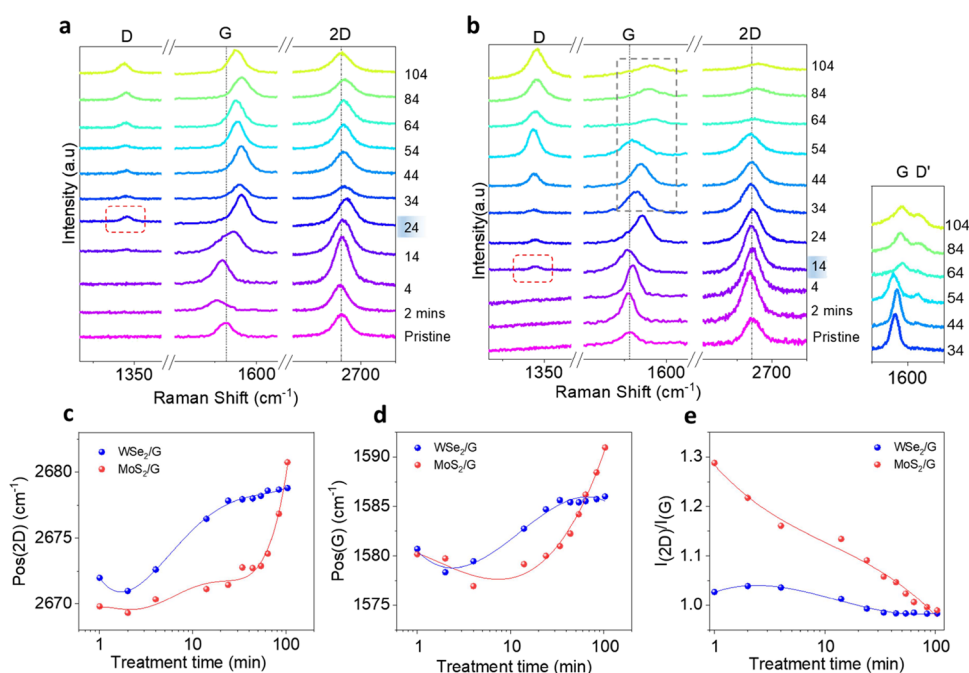
Figure 3. Raman spectra of graphene covered by monolayer (a) WSe$_2$ or (b) MoS$_2$ undergone UVO treatments up to 104 min (D peak emergence is marked in the red box). The part of the spectra indicated by small rectangles shows an enlarged scale of G and D' peaks. Time-dependent changes of (c) $2D$ and (d) G peak positions and (e) relative intensity ratio of the G and $2D$ peaks (I_{2D}/I_G).

investigate the crystal properties, and shows doping and disorder of graphene during the formation of a solid-state STCD layer.[29−37] A low laser power with a wavelength of λ_L = 532 nm is used in our Raman spectroscopy so as to avoid damaging the encapsulating TMDs and graphene. Figure 3a,b show the Raman spectra of monolayer graphene covered by monolayer TMDs (WSe$_2$ and MoS$_2$, respectively), measured at pristine state and after varied UVO treatment periods up to 104 min. In the Raman spectra of encapsulated monolayer graphene, the most prominent feature is the G peak, corresponding to the E_{2g} phonon at the Brillouin zone center,[33] which is detected at ∼1582 cm^{-1}. The D peak at ∼1350 cm^{-1} represents the existence of defects or disorders in graphene crystals.[30−33] The $2D$ peak denotes the secondary order of the D peak, lying at ∼2700 cm^{-1}.[30] The D' peak stands for another weak disorder-induced feature which appears at ∼1620 cm^{-1}.[33−35] In fact, both the G peak and $2D$ peak are strongly influenced by the carrier concentration,[34] while D peak is activated by generation of defects.[30−33] First, we attempted to monitor the doping trend, based on the changes in positions and intensities of G and $2D$ peaks.[30−33] The position of the $2D$ peak also depends on the Fermi level; nonetheless, the lattice constant also dominantly affects the position of the $2D$ peak.[38] According to our result, after oxidation, the position of the $2D$ peak blue-shifts with increasing treatment time, ∼7 and ∼11 cm^{-1}, for both WSe$_2$ and MoS$_2$-based structures, respectively, as shown in Figure 3c. This clearly indicates that those metal-oxide layers are considered as a reliable p-type dopant to graphene, similar to the previous reports.[11,39] Moreover, the position of G peak changes with doping is related to the Kohn anomaly, which correlates to the lattice constant depending on the Fermi level at the Γ point in the phonon dispersion.[38] As shown in Figure 3d, the smallest value of the G peak position is observed from the pristine sample (∼1578 cm^{-1}) and increases by 6 cm^{-1} for WSe$_2$ and 11 cm^{-1} for MoS$_2$ on monolayer graphene samples.

That indicates the increase in doping concentration for both WSe$_2$ and MoS$_2$ samples after UVO treatment,[35,40] which is quantitively investigated in the previous electrical measurement section. Moreover, the decrease in the intensity ratio of the G and $2D$ peaks (I_{2D}/I_G) to 1 after UVO treatment represented in Figure 3e also reinforces the doping effect of the SCTD layer on graphene.[34−36] We also quantitatively monitor the doping and strain of the bottom graphene flake by Raman shift as the top TMDs flakes transform into oxide layer after a prolonged UVO treatment (Figure S9). The value of n extracted from the positions of the G and $2D$ peaks in the graphene Raman spectra, in line with established methods,[41−44] is found to be ∼12 × 10^{12} cm^{-2} for the MoS$_2$-based graphene sample and ∼20 × 10^{12} cm^{-2} for the WSe$_2$-based graphene sample. These values are consistent with the doping levels obtained from Hall measurements (Figure 2), confirming the hole doping of graphene induced by the oxidized TMD flakes. Additionally, we found that no significant strain was induced in our samples after prolonged UVO treatment.

To track the generation of defects or disorders during UVO treatment of both types of samples, it is important to investigate the appearance of D peak as above-mentioned. The pristine monolayer graphene shows a defect-free crystal structure after encapsulating the monolayer TMDs, confirmed by Raman spectra shown in Figure 3a,b. No defect generation is observed in the lattice of the monolayer graphene covered by WSe$_2$ (MoS$_2$) after 24 (14) min of UVO treatment, which is proved by the absence of D or D' peaks. Another set of Raman spectra shown in Figure S10 supports the reproducibility of all the milestones for the oxidation process proposed in our work. At this stage, we observed the difference between the two types of samples. For the WSe$_2$-based device, the defects are generated after 24 min of UVO treatment, at which, the WO$_x$ layer is formed. Thus, the degradation of the transfer curve of the WSe$_2$-based device (after 24 min of UVO

treatments) shown in Figure 1b is due to the generation of defects after the formation of the WO_x layer (confirmed by the disappearance of the vibration mode of WSe_2 after ~24 min UVO treatment shown in Figures S4a and S5). On the other hand, for the MoS_2 encapsulated graphene, defects are generated after ~14 min UVO treatment, at which the top MoS_2 layer is still sustained (Figures S4b and S5), resulting in the degradation of the on-state of the device. Additionally, Raman mapping of graphene covered by WO_x and MoO_x is also performed to obtain a clear evaluation of the uniformity of the oxidation and doping process. Figure S11 shows the intensity mapping of the G and $2D$ peaks of WSe_2-covered graphene before and after doping, which suggests that the structural and vibrational properties of the graphene covered by WSe_2 have been maintained consistently across the mapped area, even after doping. Meanwhile, the oxidation and doping process has not occurred uniformly across the graphene under MoS_2, proven by the appearance of small patterns with yellow color (indicating lower intensity) on the surface (Figure S12). This is strong evidence that WO_x provides better protection capability to the underlayer graphene compared to MoO_x. This indicates the oxidation process of MoS_2 is not self-limiting,[37] leading to the poor protection of top-layer MoS_2 to bottom graphene. This phenomenon is consistent with previous studies about UVO treatment of MoS_2 flakes.[37,45−49]

To explain this observation, it is crucial to consider the quality of the TMDs flake in relation to their oxidation behaviors. Oxidation behaviors of MoS_2 and WSe_2 can be influenced by the crystalline quality including vacancies, dislocation energy, or melting point. The challenges can be ascribed to the significant disparity in kinetic energy barriers during the process of oxygen dissociative adsorption between pristine MoS_2 crystal (with a barrier of 1.59 eV) and defective MoS_2 with sulfur vacancies (which has a lower barrier of 0.8 eV).[48] Meanwhile, Liu et al. reported that the oxygen atom is more difficult to adsorb on the vacancies of WSe_2 crystal, which possibly leads to a more homogeneous oxidation process of WSe_2-based graphene.[49] Besides, the superior passivation effect of the WO_x layer can be attributed to several other factors. First, the higher dislocation energy of W−O bonds, measured at 720 kJ mol^{-1}, surpasses that of Mo−O bonds at 597 kJ mol^{-1}.[47] Additionally, the considerably higher melting point of WO_x (1473 °C) in comparison to MoO_x (795 °C) further contributes to its effectiveness as a passivating layer.[21] These combined factors contribute to the differences in oxidation behaviors and passivation effects observed between WSe_2- and MoS_2-based graphene samples.

To quantitatively probe the defects generated in TMDs encapsulated graphene lattice after UVO treatment, we thoroughly study the D peak of graphene and evaluate the defect density (n_D). The intensity of the D peak is proportional to the number of disorders (which can be point defects or crystallite boundaries) in the samples. The average n_D of the graphene lattice can be calculated from the intensity ratio between D and G peaks (I_D/I_G), as depicted in Figure 4. The defect density in the graphene can be estimated in the following equation:[50−52]

$$n_D = \frac{2.4 \times 10^{22}}{\lambda_L^4} \times \frac{I_D}{I_G} \qquad (4)$$

where λ_L is the wavelength of the Raman laser source (532 nm). Figure 3 shows no defects of graphene detected before
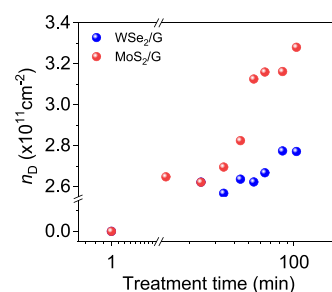
Figure 4. Density of defect in the graphene lattice during UVO treatment.

~24 and ~14 min in WSe_2- and MoS_2-based samples, respectively. Further UVO exposure results in the appearance of a D peak at ~1350 cm^{-1} for both types of TMDs encapsulated graphene flakes. Based on eq 4, we extract the defect density by using D peak intensity over prolonged UVO treatment times, as depicted in Figure 4. For the WSe_2-based graphene flake, the defect density is roughly 2.8×10^{11} cm^{-2} regardless of the treatment time of up to 134 min. In contrast, the MoS_2-based sample shows an increase in defect density up to 3.3×10^{11} cm^{-2} over the same treatment duration. Moreover, we simultaneously observed a decrease in the intensity of the G peak together with a $2D$ peak during that UVO treatment for MoS_2-covered graphene (Figure S13a,b), which is in sharp difference with steady G and $2D$ peaks of WSe_2-covered graphene. In addition, in Figure 3, the D' peak, which is split from the G peak, is less intense than the D peak but clearly exhibits in our Raman spectra of MoS_2-based graphene when increasing UVO treatment time. The D' peak correlates to defects in graphene lattice beside the D peak. On the other hand, no D' peak is observed in the Raman spectra of the WSe_2-based sample. The emergence of the D' peak indicates that the graphene layer covered by MoS_2 gets more defects than that covered by WSe_2 after prolonged UVO treatment.[33−35] The suppression of the main vibration mode together with the appearance of the defective D (D') peak of the MoS_2-based graphene after 14 (34) minutes of UVO treatment confirmed an unfavorable protecting effect of the oxidized MoS_2 to the bottom graphene flake. Meanwhile, the oxidized WSe_2 shows better protection, which prevents UVO treatment from inducing unexpected defects and limiting device performance.

Besides Raman spectra, selected area electron diffraction (SAED) patterns from TEM analysis are also effective tools for examining the quality of materials. To investigate the quality of the underlying graphene sheet during UVO treatment, we prepared three types of samples for TEM analysis: pristine graphene without UVO treatment, WSe_2-covered graphene, and MoS_2-covered graphene after UVO treatments of 50 min. Prior to transferring the oxide-covered graphene sheets onto the TEM grid, the top oxide layer was removed by dipping the samples in KOH for 10 s. This preliminary treatment enabled clear observation of the surface of the graphene sheets covered by oxide layers using TEM. The crystalline quality of the samples was also confirmed by the SAED pattern. The graphene sheet covered by WO_x shows a clear spot pattern, as shown in Figure 5b, which is comparable to the pattern observed for the pristine graphene flake in Figure 5a. In contrast, the graphene sheet covered by MoO_x exhibited diffused diffraction ring pattern, which is characteristic of the disordered structure of graphene (Figure 5c).[53] From the TEM
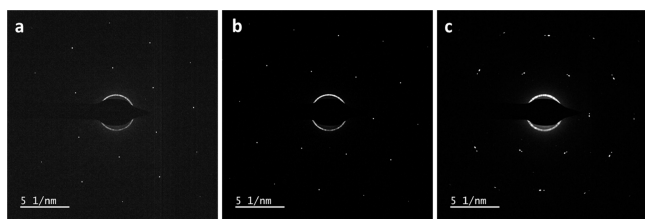
Figure 5. SAED pattern of monolayer sheets of (a) pristine, (b) WO_x and (c) MoO_x covered graphene sheet (the WO_x and MoO_x layers are removed by KOH prior to TEM measurement).

and Raman analyses, we believe that WO_x provided better protection than MoO_x during UVO treatment.

Finally, we have taken steps to enhance the practical application aspect of our work. Specifically, we have fabricated a graphene photodetector by selectively doping the graphene through a SCTD, creating a $p-n$ junction. To achieve this, we initially formed a WSe_2-based graphene FET. Subsequently, we transferred an hBN flake to cover half of the device, serving as the doping mask. To create the $p-n$ junction, we conducted UVO treatment on the exposed area for 14 min at room temperature. The device structure for the WSe_2-based graphene photodetector, fabricated using our approach, is presented in Figure 6a. The transfer curve of pristine WSe_2-based graphene FETs and $p-n$ homojunction WSe_2-based graphene photodetector is represented in Figure 6b. We assessed the effectiveness of our method by exploring the optoelectronic applications of both device types after UVO treatment by performing photoresponse measurement under λ_{laser} = 532 nm (P = 620 mW) at V_{GS} = 40 V (Figure 6c). Both types of the device show negative photoconductivity (NPC) at V_{BG} = 40 V, a behavior observed for high-mobility 2D materials such as black phosphorus, graphene, and tellurium.[54−56] The NPC observed in our device is likely attributed to electron−hole pairs generated in the top layer (WSe_2 or WO_x) under light illumination, with holes transferring to the graphene layer and electrons trapped in the top layer. This leads to hole generation in the top layer, which may compensate for the electrons generated due to bottom gating in graphene at V_{BG} = 40 V. To further highlight the effect of UVO treatment on optoelectronic properties of our device, the photocurrent against time is extracted for both device types, as depicted in Figure 6d. The photocurrent of the $p-n$ homojunction WSe_2-based graphene photodetector is notably higher than the pristine WSe_2-based graphene device counterpart for both at V_{BG} = 40 V. Therefore, this spatial patterning

of SCTDs demonstrates the potential for optoelectronic applications.

CONCLUSIONS

We applied the SCTD technique to dope monolayer graphene using an oxidized layer formed from monolayer WSe_2 (monolayer MoS_2) by UVO treatment. By tracking the appearance of the defective D peak of graphene, we can identify the optimal UVO treatment time to avoid defects or disorder generation while still obtaining a high doping concentration of 2.5×10^{13} cm^{-2}. Furthermore, by systematically tracking the Raman spectra of the samples and TEM analysis, we found that WO_x plays a better protective role on graphene than MoO_x. To enhance the practical applications of our research, we have created a graphene photodetector through selective graphene doping using SCTD, which forms a $p-n$ junction. This photodetector shows enhanced photoresponsivity compared with the intrinsic graphene device. Our findings provide guidelines for the future use of SCTD in CMOS applications.

EXPERIMENTAL SECTION

Device Fabrication Process. Monolayer graphene flakes were mechanically exfoliated with a Scotch-tape method from bulk material onto a heavily p-doped silicon substrate capped with 285 nm thick thermal SiO_2. Monolayer TMDs flakes were exfoliated by PDMS (polydimethylsiloxane) and transferred onto monolayer graphene at 60 °C. The thickness of each flake was identified by the different contrasts in the optical microscopic images and Raman spectra. The flakes were spin-coated with PMMA (poly(methyl methacrylate)) A6 with a molecule weight of 950 (Microchem) at a speed of 4000 rpm in 60 sand baked at 180 °C for 90 s, before electrode patterning via electron beam lithography. Metal contact was formed on graphene by plasma etching through the TMDs layer by inductively coupled plasma (ICP) using SF_6 with a flow rate of 30 sccm, a power of 30W, a pressure of 30 mTorr in 10s prior to contact metallization with Cr/Au (5/50 nm) by e-beam evaporation.

UVO treatment was conducted in UV-ozone cleaner at room temperature with an oxygen flow rate of 0.5 (L min^{-1}).

After UVO treatment, the graphene sheets were transferred onto the TEM grid by the PMMA-assisted wet transfer method. The PMMA/graphene stack was isolated into water after etching of the SiO_2 in KOH solution (1M) before being transferred onto the TEM grid. After the removal of PMMA by acetone, the graphene sheet on the TEM grid was ready for analysis.

The WSe_2-based graphene lateral $p-n$ junction is fabricated with first obtaining the WSe_2-based graphene FETs following the above-mentioned procedure. Subsequently, we transferred an hBN flake to cover half of the device, serving as the doping mask. To create the $p-$
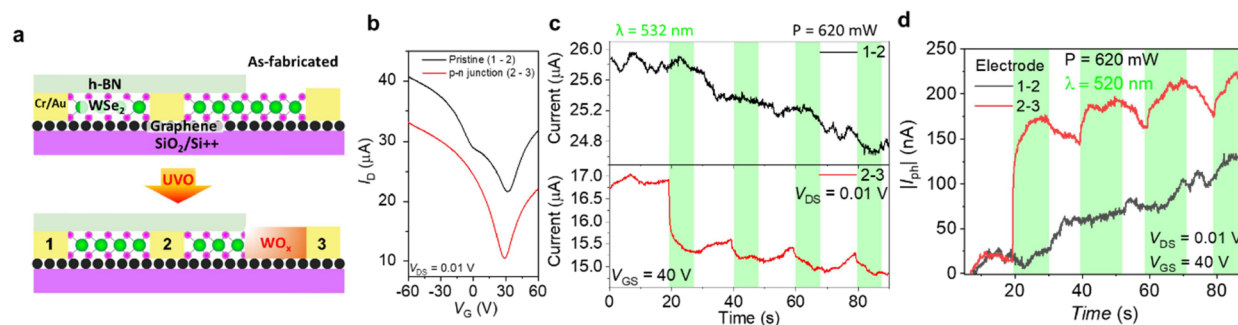
Figure 6. (a) Schematic of the WSe_2-based graphene device (1−2) and $p-n$ homojunction WSe_2-based graphene photodetector (2−3). (b) Transfer curve of the pristine WSe_2-based graphene device and the $p-n$ homojunction WSe_2-based graphene photodetector. (c) Photoresponse and (d) photocurrent of the pristine WSe_2-based graphene device and the $p-n$ homojunction WSe_2-based graphene photodetector at V_{GS} = 40 V.

n junction, we conducted UVO treatment on the exposed area for 14 min at room temperature.

Device Characterization. The electrical properties of all devices were conducted by a semiconductor parameter analyzer (Agilent 4155C) connected to a vacuum probe station (MSTECH MST-1000B) with pressure maintained at 30 mTorr at room temperature. Hall measurements were performed under high vacuum ($\sim 10^{-7}$ Torr) with a Hall-probe station (Lake Shore Cryotronics system CRX-VF) and a Keithley 4200 system.

Raman spectroscopy measurement was carried out at room temperature under atmospheric pressure with a Raman spectrometer at low laser power and wavelength of 532 nm.

TEM specimens were analyzed in Titan G2 60−300 (FEI, USA), operated at the voltage of 80 kV.

KPFM involved the connection of an AFM to an external lock-in amplifier for the application of AC bias to an AFM tip. A cantilever for KPFM with chromium and gold coatings on the conductive tip was used. AC bias (V_{AC} = 2 V) for generating resonance frequency and DC bias for the potential measurement were applied through the cantilever.

ASSOCIATED CONTENT

Supporting Information

The Supporting Information is available free of charge at https://pubs.acs.org/doi/10.1021/acsami.3c16229.

Thickness confirmation of TMDs and graphene flakes; table of comparison with different doping methods; fabrication of the oxidized TMDs-graphene FETs; comparison between UVO treatment and oxygen plasma; Raman spectra and Raman mapping of monolayer TMDs with various UVO treatment durations; on-current of oxidized TMDs encapsulated graphene FETs with various UVO treatment duration; Fermi level shift of graphene extracted by hall measurement with various UVO treatment duration; work function of WSe_2-based graphene measured by KPFM with various UVO treatment duration; extraction of n and strain by Raman shift; Raman spectra of TMDs encapsulated graphene after various UVO treatment duration; Raman mapping of WSe_2-based graphene before and after UVO treatment; Raman mapping of MoS_2-based graphene before and after UVO treatment; and Raman intensity evolution of the phonon vibration mode of TMDs encapsulated graphene with various UVO treatment duration (PDF)

AUTHOR INFORMATION

Corresponding Author

Won Jong Yoo − *SKKU Advanced Institute of Nano Technology, Sungkyunkwan University, Suwon, Gyeonggi-do 16419, Korea;* orcid.org/0000-0002-3767-7969; Email: yoowj@skku.edu

Authors

Tuyen Huynh − *SKKU Advanced Institute of Nano Technology, Sungkyunkwan University, Suwon, Gyeonggi-do 16419, Korea;* orcid.org/0009-0007-4642-8132

Tien Dat Ngo − *SKKU Advanced Institute of Nano Technology, Sungkyunkwan University, Suwon, Gyeonggi-do 16419, Korea*

Hyungyu Choi − *SKKU Advanced Institute of Nano Technology, Sungkyunkwan University, Suwon, Gyeonggi-do 16419, Korea*

Minsup Choi − *Department of Materials Science and Engineering, Chungnam National University, Daejeon 34134, Korea;* orcid.org/0000-0002-8448-4043

Wonki Lee − *Institute of Advanced Composite Materials, Korea Institute of Science and Technology (KIST), Wanju-gun, Jeolabuk-do 55324, Korea;* orcid.org/0000-0001-8945-3097

Tuan Dung Nguyen − *Center for Integrated Nanostructure Physics (CINAP), Institute for Basic Science (IBS), Suwon, Gyeonggi-do 16419, Korea*

Trang Thu Tran − *Department of Energy Science, Sungkyunkwan University, Suwon, Gyeonggi-do 16419, Korea;* orcid.org/0000-0001-8508-1652

Kwangro Lee − *SKKU Advanced Institute of Nano Technology, Sungkyunkwan University, Suwon, Gyeonggi-do 16419, Korea*

Jun Yeon Hwang − *Institute of Advanced Composite Materials, Korea Institute of Science and Technology (KIST), Wanju-gun, Jeolabuk-do 55324, Korea*

Jeongyong Kim − *Department of Energy Science, Sungkyunkwan University, Suwon, Gyeonggi-do 16419, Korea;* orcid.org/0000-0003-4679-0370

Complete contact information is available at:
https://pubs.acs.org/10.1021/acsami.3c16229

Author Contributions
[#]T.H. and T.D.N. contributed equally to this work.

Notes
The authors declare no competing financial interest.

ACKNOWLEDGMENTS

REFERENCES

(1) Luo, P.; Zhuge, F.; Zhang, Q.; Chen, Y.; Lv, Y.; Huang, Y.; Li, H.; Zhai, T. Doping Engineering and Functionalization of Two-Dimensional Metal Chalcogenides. Νανοσχαλε Ηοριζ. **2019**, 4, 26−51.
(2) Schulman, D. S.; Arnold, A. J.; Das, S. Contact Engineering for 2D Materials and Devices. Χηεμ. Σοχ. Ρεϖ. **2018**, 47, 3037−3058.
(3) Jin, Z.; Yao, J.; Kittrell, C.; Tour, J. M. Large-Scale Growth and Characterizations of Nitrogen-Doped Monolayer Graphene Sheets. ACS Nano **2011**, 5, 4112−4117.
(4) Baugher, B. W. H.; Churchill, H. O. H.; Yang, Y. F.; Jarillo-Herrero, P. Optoelectronic Devices Based on Electrically Tunable p−n Diodes in a Monolayer Dichalcogenide. Nat. Nanotechnology **2014**, 9, 262−267.
(5) Buscema, M.; Groenendijk, D. J.; Steele, G. A.; Van Der Zant, H. S. J.; Castellanos-Gomez, A. Photovoltaic Effect in Few-Layer Black Phosphorus p-n Junctions Defined by Local Electrostatic Gating. Nat. Commun. **2014**, 5, 4651.
(6) Roy, T.; Tosun, M.; Cao, X.; Fang, H.; Lien, D. H.; Zhao, P. D.; Chen, Y. Z.; Chueh, Y. L.; Guo, J.; Javey, A. Dual-Gated MoS_2/WSe_2 van der Waals Tunnel Diodes and Transistors. ACS Nano **2015**, 9, 2071−2079.
(7) Zhang, X. J.; Shao, Z. B.; Zhang, X. H.; He, Y. Y.; Jie, J. S. Surface Charge Transfer Doping of Low-Dimensional Nanostructures toward High-Performance Nanodevices. Adv. Mater. **2016**, 28, 10409−10442.
(8) Arnold, A. J.; Schulman, D. S.; Das, S. Thickness Trends of Electron and Hole Conduction and Contact Carrier Injection in Surface Charge Transfer Doped 2D Field Effect Transistors. ACS Nano **2020**, 10, 13557−13568.

(9) Borah, A.; Nipane, A.; Choi, M. S.; Hone, J.; Teherani, J. T. Low-Resistance P-Type Ohmic Contacts to Ultrathin WSe₂ by Using a Monolayer Dopant. *ACS Appl. Electron. Mater.* **2021**, *3*, 2941−2947.

(10) Liu, X.; Pan, Y.; Yang, J.; Qu, D.; Li, H.; Yoo, W. J.; Sun, J. High Performance WSe₂ p-MOSFET with Intrinsic n-Channel Based on Back-to-back p−n Junctions. *Appl. Phys. Lett.* **2021**, *118*, 233101.

(11) Choi, M. S.; Nipane, A.; Kim, B. S. Y.; Ziffer, M. E.; Datta, I.; Borah, A.; Jung, Y.; Kim, B.; Rhodes, D.; Jindal, A.; Lamport, Z. A.; Lee, M.; Zangiabadi, A.; Nair, M. N.; Taniguchi, T.; Watanabe, K.; Kymissis, I.; Pasupathy, A. N.; Lipson, M.; Zhu, X.; Yoo, W. J.; Hone, J.; Teherani, J. T. High Carrier Mobility in Graphene Doped Using a Monolayer of Tungsten Oxyselenide. *Nat. Electron.* **2021**, *4*, 731−739.

(12) Moon, I.; Lee, S.; Lee, M.; Kim, C.; Seol, D.; Kim, Y.; Kim, K. H.; Yeom, G. Y.; Teherani, J. T.; Hone, J.; Yoo, W. J. The Device Level Modulation of Carrier Transport in a 2D WSe₂ Field Effect Transistor via a Plasma Treatment. *Nanoscale* **2019**, *11*, 17368−17375.

(13) Yamamoto, M.; Dutta, S.; Aikawa, S.; Nakaharai, S.; Wakabayashi, K.; Fuhrer, M. S.; Ueno, K.; Tsukagoshi, K. Self-Limiting Layer-By-Layer Oxidation of Atomically Thin WSe₂. *Nano Lett.* **2015**, *4*, 2067−2073.

(14) Choi, M. S.; Lee, M.; Ngo, T. D.; Hone, J.; Yoo, W. J. Chemical Dopant-Free Doping by Annealing and Electron Beam Irradiation on 2D Materials. *Adv. Electron. Mater.* **2021**, *7*, No. 2100449.

(15) Shi, V.; Kahn, S.; Jiang, L.; Wang, S.-Y.; Tsai, H.-Z.; Wong, D.; Taniguchi, T.; Watanabe, K.; Wang, F.; Crommie, M. F.; Zettl, A. Reversible Writing of High-Mobility and High-Carrier-Density Doping Patterns in Two-Dimensional van der Waals Heterostructures. *Nat. Electron.* **2020**, *3*, 99−105.

(16) Curtis, L., Jr; Srour, J. R.; Chiu, K. Y. Hole and Electron Transport in SiO₂ Films. *J. Appl. Phys.* **1974**, *45*, 4506−4513.

(17) Pang, C.-S.; Hung, T. Y. T.; Khosravi, A.; Addo, R.; Wang, Q.; Kim, M. J.; Wallace, R. M. R. M.; Chen, Z. Atomically Controlled Tunable Doping in High-Performance WSe₂ Devices. *Adv. Electron. Mater.* **2020**, *6*, No. 1901304.

(18) Ngo, T. D.; Choi, M. S.; Lee, M.; Ali, F.; Hassan, Y.; Ali, N.; Liu, S.; Lee, C.; Hone, J.; Yoo, W. J. Selective Electron Beam Patterning of Oxygen-Doped WSe₂ for Seamless Lateral Junction Transistors. *Adv. Sci.* **2022**, *9*, No. 2202465.

(19) Alam, M. H.; Chowdhury, S.; Roy, A.; Wu, X.; Ge, R.; Rodder, M. A.; Chen, J.; Lu, Y.; Stern, C.; Houben, L.; Chrostowski, R.; Burlison, S. R.; Yang, S. J.; Serna, M. I.; Dodabalapur, A.; Mangolini, F.; Naveh, D.; Lee, J. C.; Banerjee, S. K.; Warner, J. H.; Akinwande, D. Wafer-Scalable Single-Layer Amorphous Molybdenum Trioxide. *ACS Nano* **2022**, *3*, 3756−3767.

(20) Ryu, G. H.; Lee, J.; Kang, D.; Jo, H. J.; Shin, H. S.; Lee, Z. Effects of Dry Oxidation Treatments on Monolayer Graphene. *2D Mater.* **2017**, *4*, No. 024011.

(21) Pei, C.; Li, X.; Fan, H.; Wang, J.; You, H.; Yang, P.; Wei, C.; Wang, S.; Shen, X.; Li, H. Morphological and Spectroscopic Characterizations of Monolayer and Few-Layer MoS₂ and WSe₂ Nanosheets under Oxygen Plasma Treatment with Different Excitation Power: Implications for Modulating Electronic Properties. *ACS Appl. Nano Mater.* **2020**, *3*, 4218−4230.

(22) Zhang, Y.; Liu, J.; Pan, Y.; Luo, K.; Yu, J.; Zang, Y.; Jia, K.; Yin, H.; Zhu, H.; Tian, H.; Wu, Z. The Evolution of MoS₂ Properties Under Oxygen Plasma Treatment and Its Application in MoS₂ Based Devices. *J. Mater. Sci.: Mater. Electron.* **2019**, *30*, 18185−18190.

(23) Giannazzo, F.; Fisichella, G.; Greco, G.; Di Franco, S.; Deretzis, I.; La Magna, A.; Bongiorno, C.; Nicotra, G.; Spinella, C.; Scopelliti, M.; Pignataro, B.; Agnello, S.; Roccaforte, F. Ambipolar MoS₂ Transistors by Nanoscale Tailoring of Schottky Barrier Using Oxygen Plasma Functionalization. *ACS Nano* **2017**, *9*, 23164−23174.

(24) Lindvall, N.; Kalabukhov, A.; Yurgens, A. Cleaning Graphene Using Atomic Force Microscope. *J. Appl. Phys.* **2012**, *111*, No. 064904.

(25) Mitta, S. B.; Choi, M. S.; Nipane, A.; Ali, F.; Kim, C.; Teherani, J. T.; Hone, J.; Yoo, W. J. Electrical Characterization of 2D Materials-Based Field-Effect Transistors. *2D Mater.* **2021**, *8*, No. 012002.

(26) Lee, D.; Lee, J. J.; Kim, Y. S.; Kim, Y. H.; Kim, J. C.; Huh, W.; Lee, J.; Park, S.; Jeong, H. Y.; Kim, Y. D.; Lee, C. H. Remote Modulation Doping in van der Waals Heterostructure Transistors. *Nat. Electron.* **2021**, *4*, 664−670.

(27) Jang, J.; Kim, J.-K.; Shin, J.; Kim, J.; Baek, K.-Y.; Park, J.; Park, S.; Kim, Y. D.; Parkin, S. S. P.; Kang, K.; Cho, K.; Lee, T. Reduced Dopant-Induced Scattering in Remote Charge-Transfer-Doped MoS₂ Field-Effect Transistors. *Sci. Adv.* **2022**, *8*, 3181.

(28) Arnold, A. J.; Schulman, D. S.; Das, S. Thickness Trends of Electron and Hole Conduction and Contact Carrier Injection in Surface Charge Transfer Doped 2D Field Effect Transistors. *ACS Nano* **2020**, *14*, 13557−13568.

(29) Yan, J.; Zhang, Y.; Kim, P.; Pinczuk, A. Electric Field Effect Tuning of Electron-Phonon Coupling in Graphene. *Phys. Rev. Lett.* **2007**, *98*, No. 166802.

(30) Casaragi, C.; Pisana, S.; Novoselov, K. S.; Geim, A. K.; Ferrari, A. C. Raman Fingerprint of Charged Impurities in Graphene. *Appl. Phys. Lett.* **2007**, *91*, 233108.

(31) Ferrari, A. C.; Meyer, J. C.; Scardaci, V.; Casiraghi, C.; Lazzeri, M.; Mauri, F.; Piscanec, S.; Jiang, D.; Novoselov, K. S.; Geim, A. K. Raman Spectrum of Graphene and Graphene Layers. *Phys. Rev. Lett.* **2006**, *97*, No. 187401.

(32) Lucchese, M. M.; Stavale, F.; Ferreira, E. H. M.; Vilani, C.; Moutinho, M. V. O.; Capaz, R. B.; Achete, C. A.; Jorio, A. Quantifying Ion-Induced Defects and Raman Relaxation Length in Graphene. *Carbon* **2010**, *48*, 1592−1597.

(33) Cancado, L. G.; Jorio, A.; Martins Ferreira, E. H.; Stavale, F.; Achete, C. A.; Capaz, R. B.; Moutinho, M. V. O.; Lombardo, A.; Kulmala, T. S.; Ferrari, A. C. Quantifying Defects in Graphene via Raman Spectroscopy at Different Excitation Energies. *Nano Lett.* **2011**, *11*, 3190−3196.

(34) Das, A.; Pisana, S.; Chakraborty, B.; Saha, S. K.; Waghmare, U. V.; Novoselov, K. S.; Krishnamurthy, H. R.; Geim, A. K.; Ferrari, A. C.; Sood, A. K. Monitoring Dopants by Raman Scattering in an Electrochemically Top-Gated Graphene Transistor. *Nat. Nanotechnol.* **2008**, *3*, 210−215.

(35) Pisana, S.; Lazzeri, M.; Casiraghi, C.; Novoselov, K. S.; Geim, A. K.; Ferrari, A. C.; Mauri, F. Breakdown of the Adiabatic Born−Oppenheimer Approximation in Graphene. *Nat. Mater.* **2007**, *6*, 198−201.

(36) Stampfer, C.; Molitor, F.; Graf, D.; Ensslin, K.; Jungen, A.; Hierold, C.; Wirtz, L. Raman Imaging of Doping Domains in Graphene on SiO₂. *Appl. Phys. Lett.* **2007**, *91*, 241907.

(37) Nipane, A.; Choi, M. S.; Sebastian, P. J.; Yao, K.; Borah, A.; Deshmukh, P.; Jung, Y.; Kim, B.; Rajendran, A.; Kwock, K. W. C.; Zangiabadi, A.; Menon, V. M.; Schuck, P. J.; Yoo, W. J.; Hone, J.; Teherani, J. T. Damage-Free Atomic Layer Etch of WSe₂: A Platform for Fabricating Clean Two-Dimensional Devices. *ACS Appl. Mater. Interfaces* **2021**, *13*, 1930−1942.

(38) Beams, R.; Cancado, L. G.; Novotny, L. Raman Character-ization of Defects and Dopants in Graphene. *J. Phys.: Condens. Matter* **2015**, *27*, No. 083002.

(39) Vaziri, S.; Chen, V.; Cai, L.; Jiang, Y.; Chen, M. E.; Grady, R. W.; Zheng, X.; Pop, E. Ultrahigh Doping of Graphene Using Flame-Deposited MoO₃. *IEEE Electron Device Lett.* **2020**, *10*, 1592−1595.

(40) Ott, A.; Verzhbitskiy, I. A.; Clough, J.; Eckmann, A.; Georgiou, T.; Casiraghi, C. Tunable D Peak in Gated Graphene. *Nano Res.* **2014**, *7*, 338−344.

(41) Giannazzo, F.; Shtepliuk, I.; Ivanov, I. G.; Iakimov, T.; Kakanakova-Georgieva, A.; Schilirò, E.; Fiorenza, P.; Yakimova, R. Probing the uniformity of hydrogen intercalation in quasi-free-standing epitaxial graphene on SiC by micro-Raman mapping and conductive atomic force microscopy. *Nanotechnology* **2019**, *30*, 284003.

(42) Armano, A.; Buscarino, G.; Cannas, M.; Gelardi, F. M.; Giannazzo, F.; Schilirò, F.; Agnello, S. Monolayer Graphene Doping and Strain Dynamics Induced by Thermal Treatments in Controlled Atmosphere. *Carbon* **2018**, *127*, 270−279.

(43) Panasci, S. E.; Schilirò, E.; Greco, G.; Cannas, M.; Gelardi, F. M.; Agnello, S.; Roccaforte, F.; Giannazzo, F. Strain, Doping, and Electronic Transport of Large Area Monolayer MoS$_2$ Exfoliated on Gold and Transferred to an Insulating Substrate. *ACS Appl. Mater. Interfaces* **2021**, *13*, 31248−31259.

(44) Lee, J. E.; Ahn, G.; Shim, J.; Lee, Y. S.; Ruy, S. Optical Separation of Mechanical Strain from Charge Doping in Graphene. *Nat. Commun.* **2012**, *3*, 1024.

(45) Liu, J.; Sun, K.; Zheng, X.; Wang, S.; Lian, S.; Deng, C.; Xie, H.; Zang, X.; Gao, Y.; Song, F.; Huang, H. Evolutions of Morphology and Electronic Properties of Few-Layered MoS$_2$ Exposed to UVO. *Results Phys.* **2020**, *19*, No. 103634.

(46) Ma, X.; Zhang, J.; Sun, Y.; Wu, C.; Geng, G.; Zhang, J.; Wu, E.; Xu, L.; Wu, S.; Hu, X.; Liu, J. Engineering of Oxidized Line Defects on CVD-Grown MoS$_2$ Flakes. *ACS Appl. Mater. Interfaces* **2022**, *14*, 47288−47299.

(47) Azcatl, A.; Kc, S.; Peng, X.; Lu, N.; McDonnell, S.; Qin, X.; de Dios, F.; Addou, R.; Kim, J.; Kim, M. J.; Cho, K.; Wallace, R. M. HfO$_2$ on UV−O$_3$ Exposed Transition Metal Dichalcogenides: Interfacial Reactions Study. *2D Mater.* **2015**, *2*, No. 014004.

(48) Kc, S.; Longo, R. C.; Wallace, R. M.; Cho, K. Surface Oxidation Energetics and Kinetics on MoS$_2$ Monolayer. *J. Appl. Phys.* **2015**, *117*, 135301.

(49) Liu, H.; Han, N.; Zhao, J. Atomistic Insight into the Oxidation of Monolayer Transition Metal Dichalcogenides: from Structures to Electronic Properties. *RSC Adv.* **2015**, *5*, 17572−17581.

(50) Krishnamoorthy, K.; Veerapandian, M.; Yun, K.; Kim, S.-J. The Chemical and Structural Analysis of Graphene Oxide with Different Degrees of Oxidation. *Carbon* **2013**, *53*, 38−49.

(51) Sharma, R.; Chadha, N.; Saini, P. Determination of Defect Density, Crystallite Size and Number of Graphene Layers in Graphene Analogues Using X-Ray Diffraction and Raman Spectroscopy. *Indian J. Pure Appl. Phys.* **2017**, *55*, 625−629.

(52) Cancado, L. G.; Takai, K.; Enoki, T.; Endo, M.; Kim, Y. A.; Mizusaki, H.; Jorio, A.; Coelho, L. N.; Magalhães-Paniago, R.; Pimenta, M. A. General Equation for the Determination of the Crystallite Size La of Nanographite by Raman Spectroscopy. *Appl. Phys. Lett.* **2006**, *88*, 163106.

(53) Wang, G.; Zhang, M.; Zhu, Y.; Ding, G.; Jiang, D.; Guo, Q.; Liu, S.; Xie, X.; Chu, P. K.; Di, Z.; Wang, X. Direct Growth of Graphene Film on Germanium Substrate. *Sci. Rep.* **2013**, *3*, 2465−2471.

(54) Miao, J.; Song, B.; Li, Q.; Cai, L.; Zhang, S.; Hu, W.; Dong, L.; Wang, C. Photothermal Effect Induced Negative Photoconductivity and High Responsivity in Flexible Black Phosphorus Transistors. *ACS Nano* **2017**, *11*, 6048−6056.

(55) Konstantatos, G.; Badioli, M.; Gaudreau, L.; Osmond, J.; Bernechea, M.; De Arquer, F. P. G.; Gatti, F.; Koppens, F. H. L. Hybrid Graphene-Quantum Dot Phototransistors with Ultrahigh Gain. *Nat. Nanotechnol.* **2012**, *7*, 363−368.

(56) Nguyen, D. A.; Cho, S.; Park, S.; Park, D. Y.; Suh, H. C.; Jeong, M. S.; Bach, T. P. A; Kim, H.; Im, H. Tunable Negative Photoconductivity in Encapsulated Ambipolar Tellurene for Functional Optoelectronic Device Applications. *Nano Energy* **2023**, *113*, No. 108552.